Supporting information

Nitrogen- and carbonyl-rich conjugated small-molecule organic cathode for high-performance sodium-ion batteries

Hsuan-Cheng Kuan,‡[a] Nhu T. H. Luu,‡[a] Alexander S. Ivanov,[b] Teng-Hao Chen,[c] Ilja Popovs,[b] Jui-Chin Lee[d] and Watchareeya Kaveevivitchai*[a]

---

a *Department of Chemical Engineering*
and Hierarchical Green-Energy Materials (Hi-GEM) Research Center
National Cheng Kung University
No.1 University Rd., Tainan City 70101, Taiwan

b *Chemical Sciences Division, Oak Ridge National Laboratory*
Oak Ridge, P.O. Box 2008, TN 37831, USA

c *School of Pharmacy, National Cheng Kung University*
No.1 University Rd., Tainan City 70101, Taiwan

d *Core Facility Center*
National Cheng Kung University
No.1 University Rd., Tainan City 70101, Taiwan

‡ *These authors contributed equally to this work.*

*To whom correspondence should be addressed. E-mail: wkaveechai@mail.ncku.edu.tw

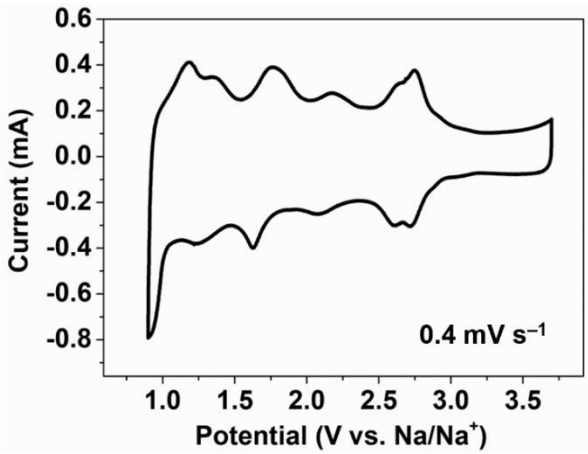

Fig. S1 Cyclic voltammetry (CV) plot of Na/HATAQ with a scan rate of 0.4 mV s^{-1}.

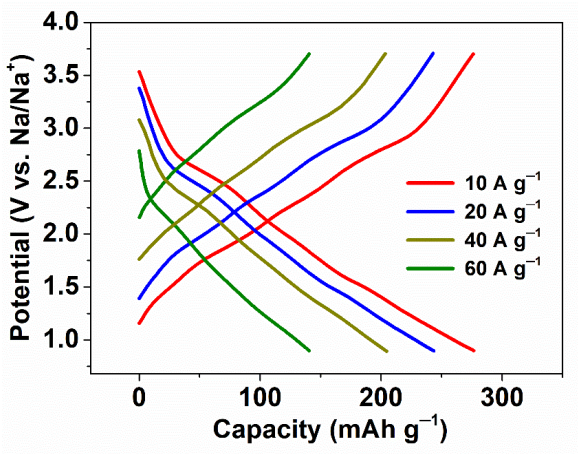

Fig. S2 Discharge/charge profiles of Na/HATAQ cells at different current densities ranging from 10 to 60 A g^{-1}.

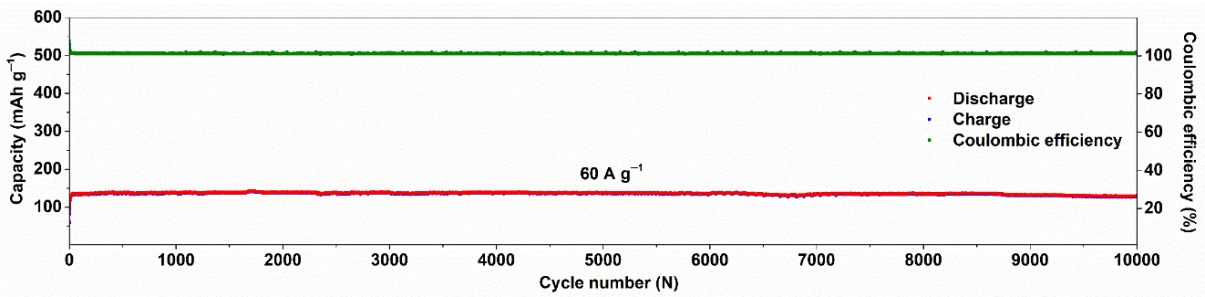

Fig. S3 Long-term cycling performance of HATAQ at 60 A g^{-1} for 10000 cycles together with Coulombic efficiency.

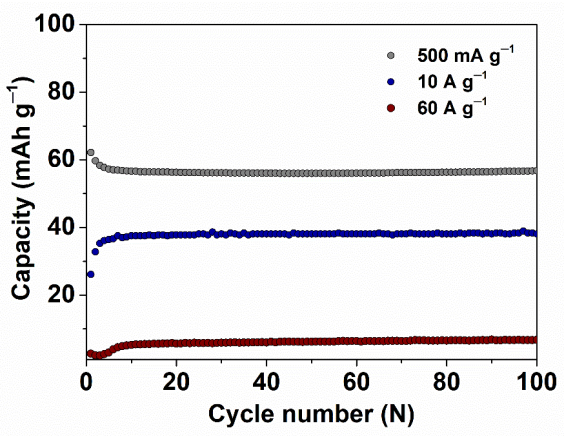

Fig. S4 Electrochemical properties of the conductive carbon (electrode ratio: Ketjen black : PVDF = 9:1, with mass loading of Ketjen black ~1.5 mg cm^{-2}) at 0.5, 10 and 60 A g^{-1} with 0.9 M $NaPF_6$ in diethylene glycol dimethyl ether (DEGDME) as electrolyte and Na metal as anode. The delivered capacity of Ketjen black at this electrode ratio is estimated to be ~56 mAh g^{-1} at 0.5 A g^{-1} (between 0.9–3.7 V). At high rates, the capacity contribution from Ketjen black is considered to be almost negligible within this voltage window.

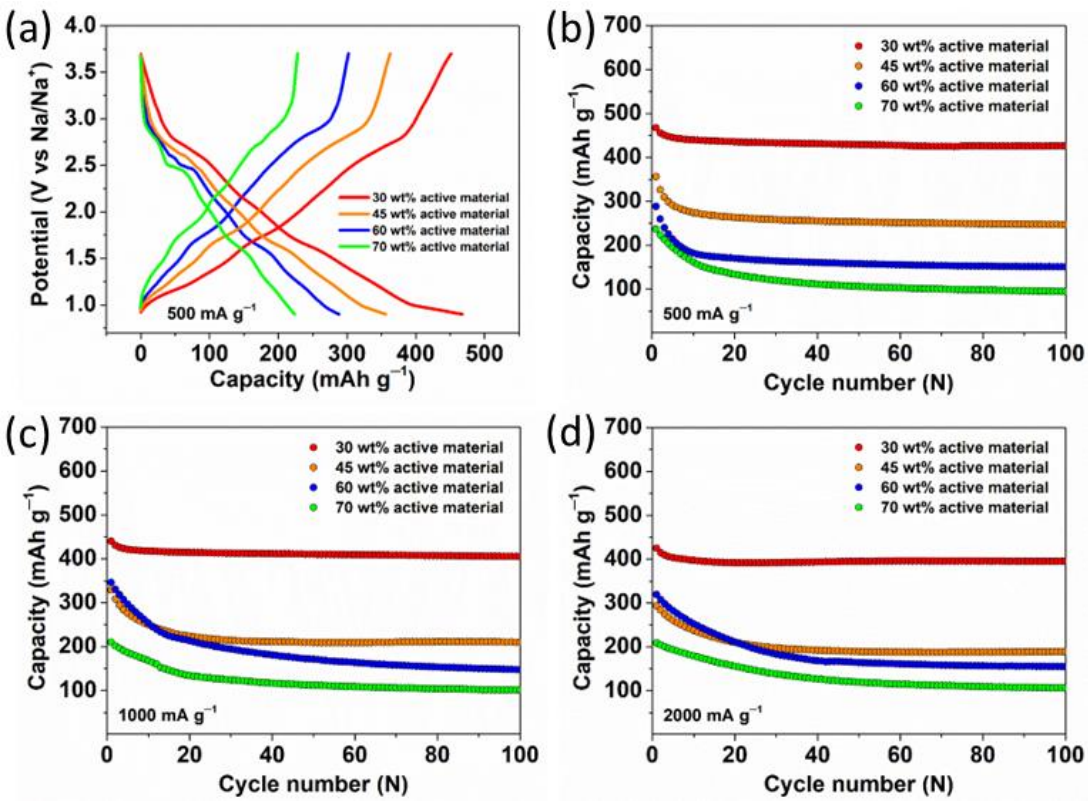

Fig. S5 (a) Discharge/charge profiles and (b) capacity retention plots of HATAQ electrodes with different amounts of active material at 500 mA g^{-1} (PVDF was kept constant at 10 wt%). (c) and (d) Retention plots of various electrode ratios at 1000 and 2000 mA g^{-1}, respectively.

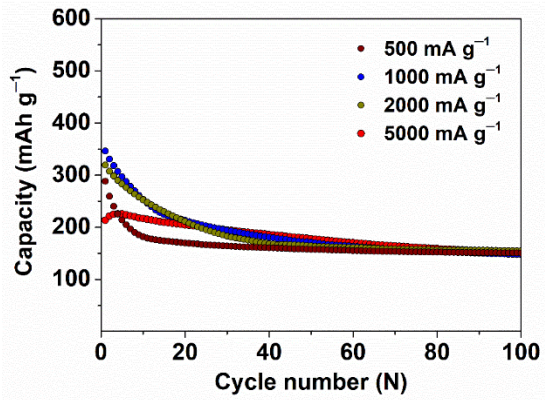

Fig. S6 Capacity retention plots of HATAQ (active material : Ketjen black : PVDF = 6:3:1) at rates of 500 to 5000 mA g^{-1}.

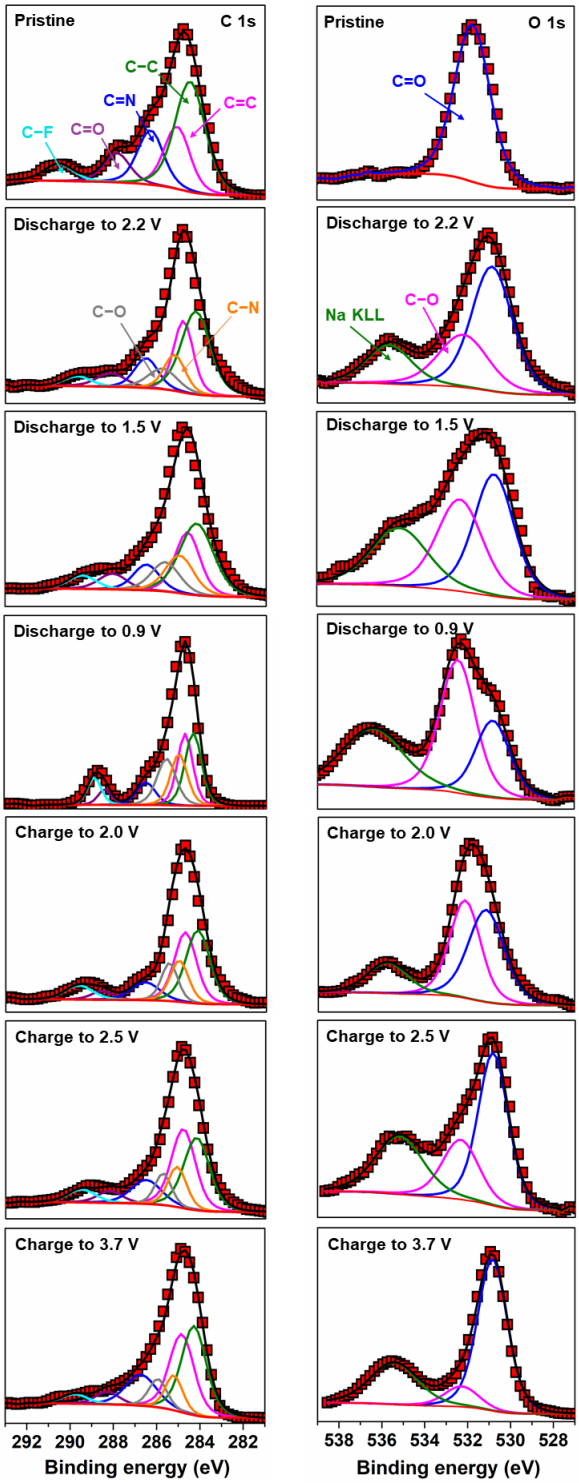

Fig. S7 Deconvolution of the high-resolution X-ray photoelectron spectroscopy (XPS) spectra of HATAQ electrodes cycled at 200 mA g^{-1}: (Left) C 1s; (Right) O 1s.

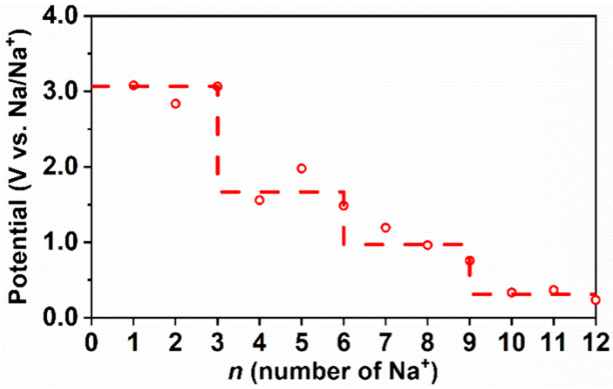

Fig. S8 Discharge profile corresponding to HATAQ sodiation steps obtained from density functional theory (DFT) calculations. Empty red circles denote the calculated reduction potentials, while the red dashed line connects the average redox values for the three-electron transfer step and serves as a guide to the eye to formally divide the HATAQ sodiation into four distinct processes (four sequential additions of three Na).

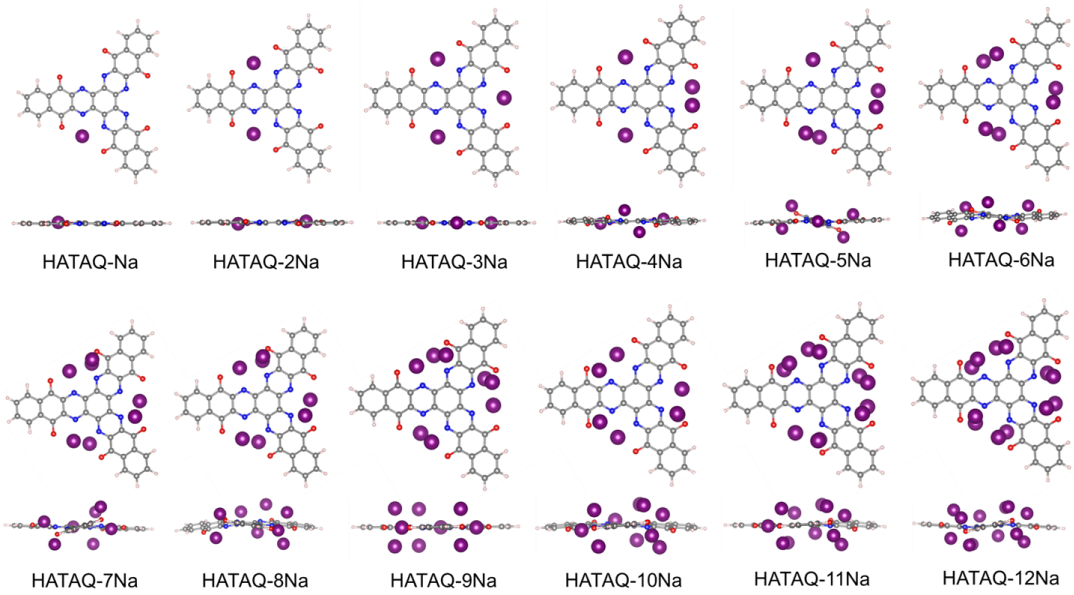

Fig. S9 Top and side views of the DFT optimized global minimum structures for the HATAQ-*n*Na (*n* = 1-12) complexes at the B3LYP/6-31+G(d,p)//IEF level of theory. Colour scheme: C, grey; H, white; N, blue; O, red; Na, purple.

Table S1. Calculated binding energies (BEs) and redox potentials at the B3LYP/6-31+G(d,p)//IEF level in DME solvent. BEs were calculated for the consecutive sodiation processes according to the following equation: BE = $E_{HATAQ\text{-}nNa} - (E_{HATAQ\text{-}(n\text{-}1)Na} + E_{Na})$, where $E_{HATAQ\text{-}nNa}$, $E_{HATAQ\text{-}(n\text{-}1)Na}$, and E_{Na} are the sum of electronic and zero-point energies (eV) of the final and initial sodiated states of the HATAQ molecule, and sodium atom, respectively; *n* is the number of Na/electrons transferred in the process.

Sodiation steps	**HATAQ → HATAQ1Na**	**HATAQ1Na → HATAQ2Na**	**HATAQ2Na → HATAQ3Na**	**HATAQ3Na → HATAQ4Na**	**HATAQ4Na → HATAQ5Na**	**HATAQ5Na → HATAQ6Na**
BE, eV	-3.39	-3.19	-3.57	-1.93	-2.24	-1.79
Potential, V (vs. Na/Na$^+$)	3.08	2.83	3.28	1.56	1.98	1.47

Sodiation steps	**HATAQ6Na → HATAQ7Na**	**HATAQ7Na → HATAQ8Na**	**HATAQ8Na → HATAQ9Na**	**HATAQ9Na → HATAQ10Na**	**HATAQ10Na → HATAQ11Na**	**HATAQ11LNa → HATAQ12Na**
BE, eV	-1.62	-1.22	-1.07	-0.70	-0.69	-0.44
Potential, V (vs. Na/Na$^+$)	1.28	0.87	0.75	0.33	0.38	0.22

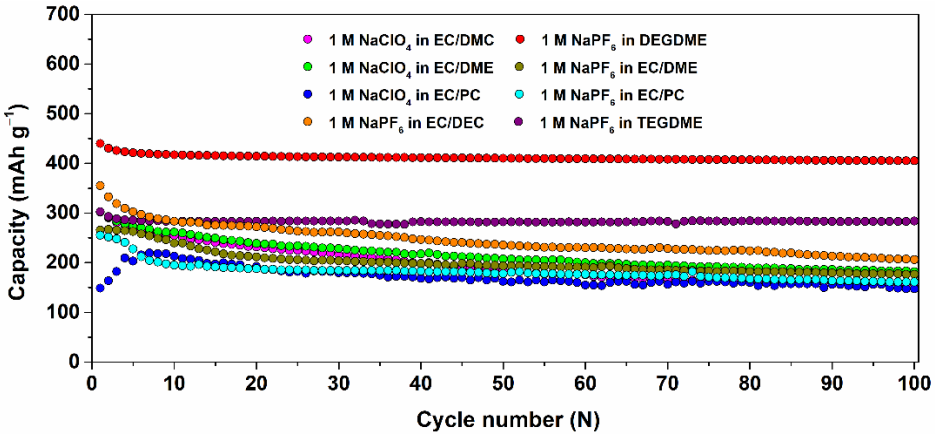

Fig. S10 Cycling performance of HATAQ electrodes at 1 A g^{-1} in various 1 M Na organic electrolytes (EC: ethylene carbonate; DMC: dimethyl carbonate; DME: dimethoxyethane, also known as monoglyme or ethylene glycol dimethyl ether; PC: propylene carbonate; DEC: diethyl carbonate; DEGDME: diethylene glycol dimethyl ether or diglyme; TEGDME: tetraethylene glycol dimethyl ether or tetraglyme).

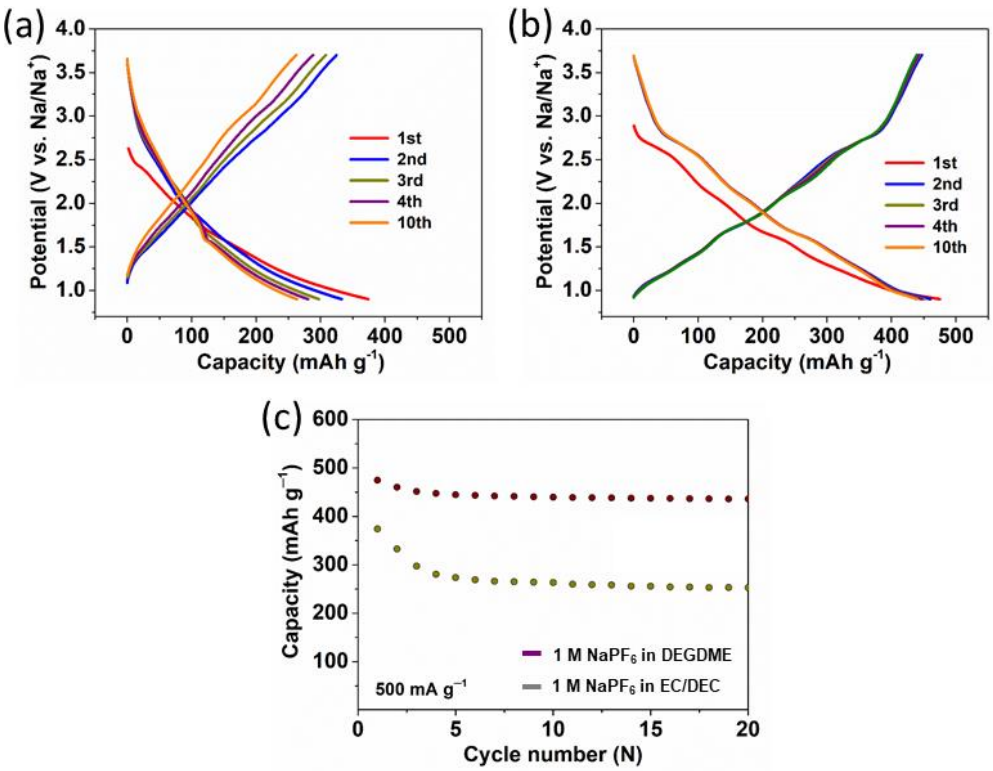

Fig. S11 (a) and (b) Discharge/charge profiles of HATAQ for the first ten cycles at 500 mA g^{-1} in 1 M $NaPF_6$ in EC/DEC and DEGDME electrolyte, respectively. (c) Capacity retention of the compound in the two electrolytes showing far superior performance in the ether-based system.

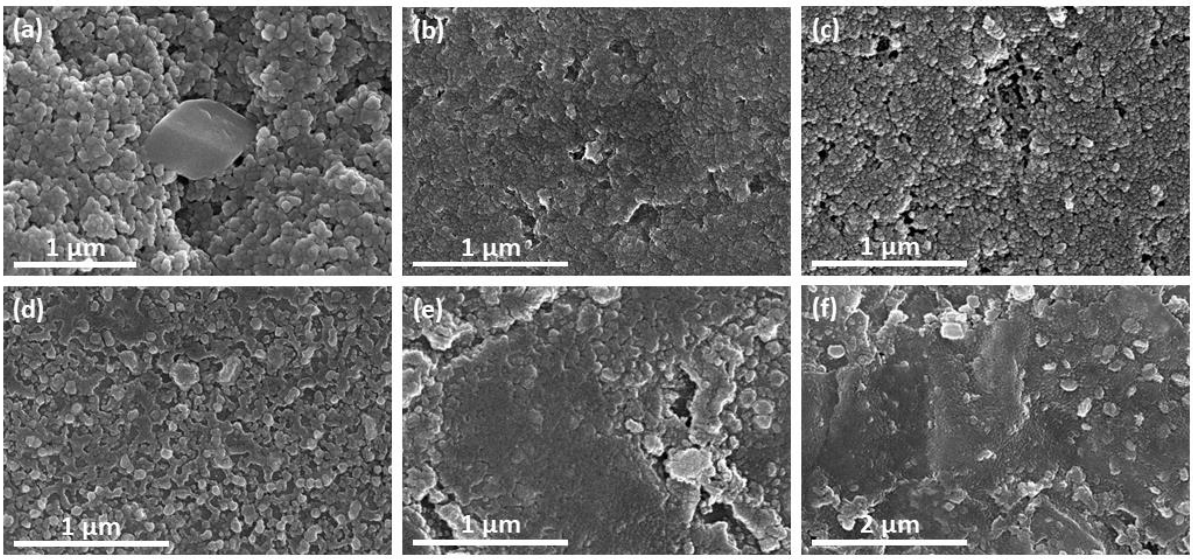

Fig. S12 Scanning electron microscopy (SEM) images of HATAQ electrodes at various conditions: (a) pristine electrode; (b) and (c) electrodes in 1 M $NaPF_6$ in DEGDME after 1 and 20 cycles, respectively; (d) electrode in 1 M $NaPF_6$ in EC/DEC after 1 cycle; (e) and (f) electrodes in 1 M $NaPF_6$ in EC/DEC after 20 cycles with two different magnifications. All the electrodes were cycled at the rate of 500 mA g^{-1}.

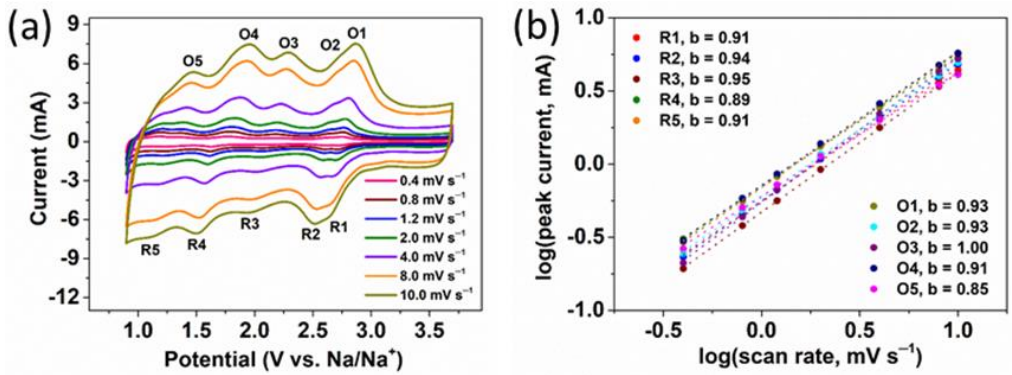

Fig. S13 (a) CV curves of HATAQ electrode at different scan rates in 0.9 M $NaPF_6$ in DEGDME. (b) Relationship between log(i, peak current) vs log(v, scan rate) of the CV peaks in (a). The analysis of charge storage process was performed with b values calculated from $i = av^b$. The measured current i is fit to a power law with scan rate v. b can be determined from the slope of the log i vs. log v. According to these results, the Faradaic charge storage associated with the peak maxima in CV of HATAQ has a significant capacitive contribution: b = 0.5 indicating traditional diffusion dominated charge storage, while b = 1 indicating capacitor-like charge storage.[1,2]

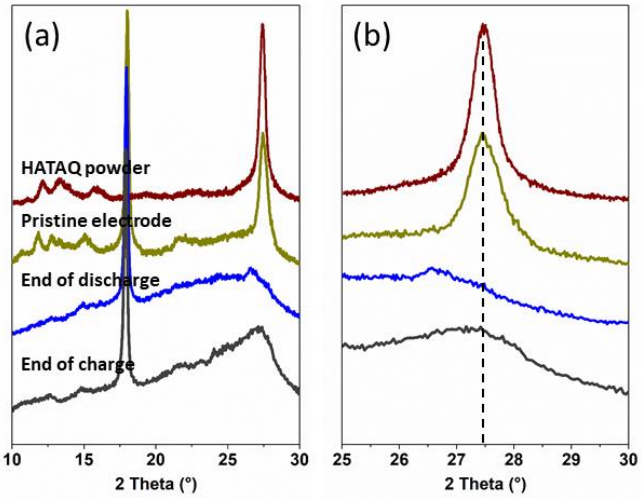

Fig. S14 Ex-situ powder X-ray diffraction (PXRD) patterns of HATAQ electrodes at the end of discharge (0.9 V) and end of charge (3.7 V) at the rate of 200 mA g^{-1} in comparison with those of HATAQ powder and pristine HATAQ electrode. (a) and (b) show two different 2θ ranges. The peak at approximately 18º belongs to PTFE polymer binder. It is obvious that the peak at ~27º slightly shifts toward a lower 2θ when the HATAQ electrode is discharged and subsequently moves back to a higher angle during charge. This may be explained by an increase in the interlayer spacing of HATAQ structure due to the interactions with Na ions during discharge and a decrease of the interlayer distance due to Na-ion extraction during charge.

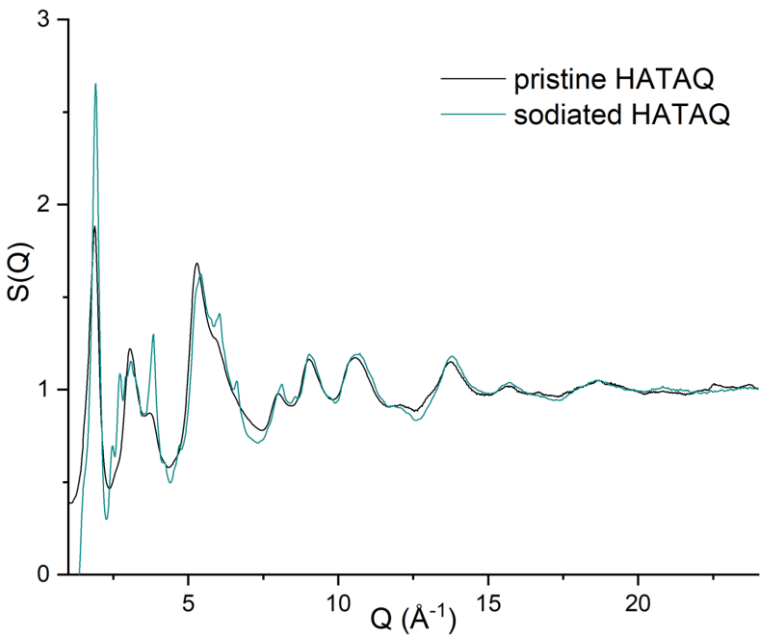

Fig. S15 Structure functions, S(Q)'s, for the pristine HATAQ (black) and fully discharged HATAQ (teal) samples. The pair distribution functions (PDFs) reported in the main text were obtained by the Fourier transform of the respective S(Q)s.

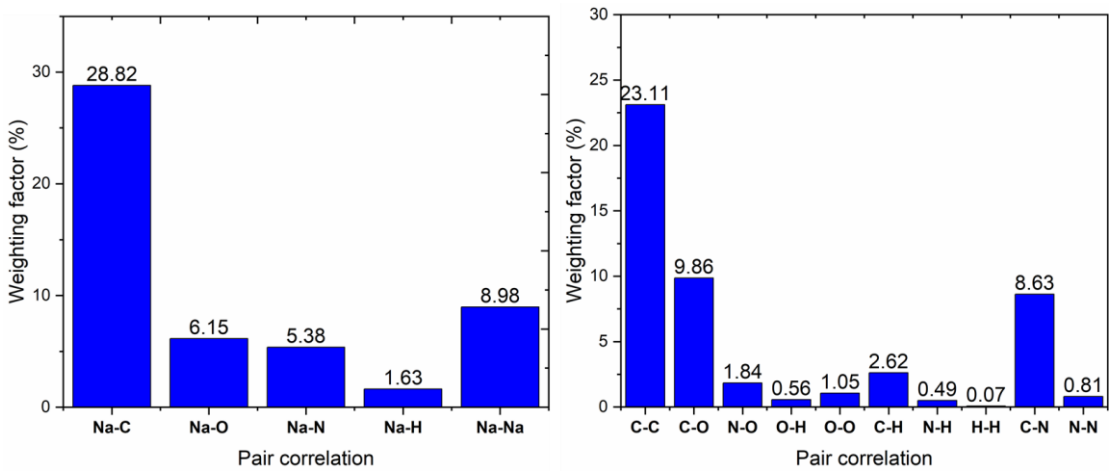

Fig. S16 The relative X-ray weighting factors ($w_{\alpha\beta}(Q) = \frac{(2-\delta_{\alpha\beta})c_\alpha c_\beta f_\alpha(Q) f_\beta(Q)}{[\sum_\alpha c_\alpha f_\alpha(Q)]^2}$, where $f_\alpha(Q)$, $f_\beta(Q)$ are Q-dependent X-ray atomic form factors, c_α, c_β are molar fractions of species α and β, respectively, and $\delta_{\alpha\beta}$ is one for $\alpha=\beta$ and zero for $\alpha \neq \beta$) calculated at Q = 0 for the atomic pair correlations in the Na-HATAQ system. As can be seen, most of the scattering comes from the pairs containing Na, C, O, and N and thus the X-ray scattering patterns in Fig. 5 (main text) are primarily dominated by Na-C, C-C, C-O, C-N, Na-Na, Na-O, and Na-N correlations.

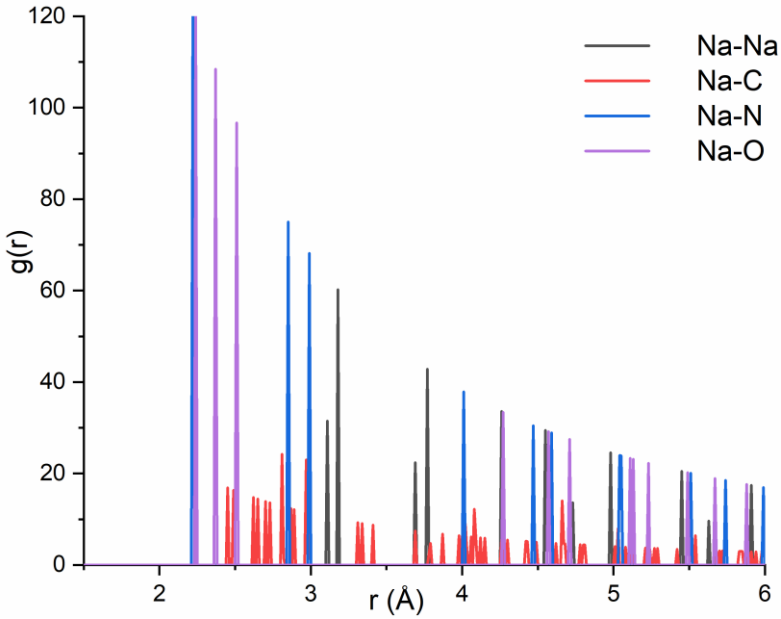

Fig. S17 Partial radial distribution functions, g(r), (not X-ray weighted) for sodium-HATAQ pair correlations from a DFT optimized periodic structure of the fully sodiated HATAQ.

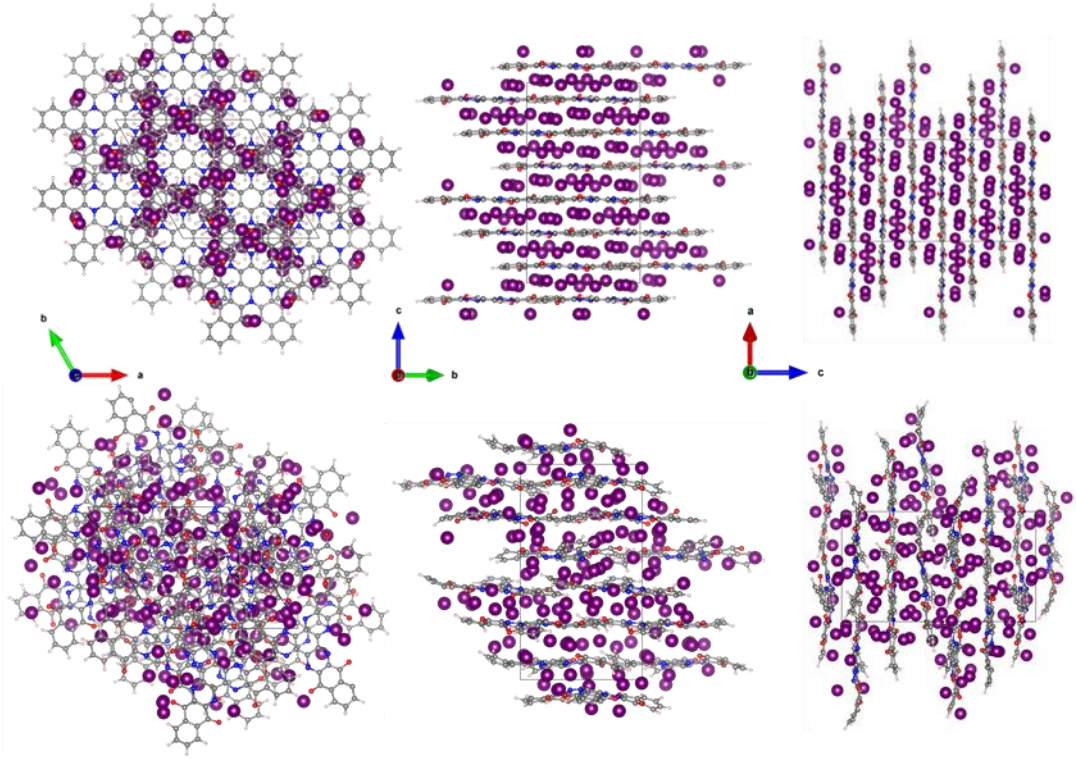

Fig. S18 Structural changes of the fully sodiated HATAQ before (top) and after (bottom) 6 ps of *ab initio* molecular dynamics (MD) simulations at T = 450 K.

Activation energy calculation

The temperature-dependent EIS measurements can be used to obtain the interfacial and charge-transfer resistances, R_{SEI} *and* R_{ct}, respectively, by fitting the Nyquist plots. The activation energies can then be estimated by using the equation below:[3-6]

$$\frac{1}{R_{(ct,SEI)}} = A_0 e^{-E_a/RT} \qquad (1)$$

where A_0 is a pre-exponential constant, R is the standard gas constant, and E_a is the activation energy. From the slope of the Arrhenius behaviors between $\log(R^{-1}_{(ct,SEI)})$ and 1/T, the activation energy for charge transfer process ($E_{a,ct}$) and the activation energy across SEI layer ($E_{a,SEI}$) may be calculated:

$$E_a = -19.144 \times \text{slope (kJ mol}^{-1}) \qquad (2)$$

Kinetic analysis (CV)

The discharge/charge kinetics of HATAQ in Na cells as shown in Fig. 4d (main text) was investigated by analyzing the CV data at various scan rates. To quantitatively differentiate the contribution of the capacitive and diffusion-controlled elements to the overall capacity, the relationship $i = av^b$ can be divided into two terms: the capacitive effects ($k_1 v$) and diffusion-limited effects ($k_2 v^{1/2}$) as follows: $i = k_1 v + k_2 v^{1/2}$, where i is the current (A) at a fixed potential and a corresponding scan rate v (V s^{-1}). By plotting $v^{1/2}$ vs $i/v^{1/2}$, k_1 and k_2 are derived from the slope and the y-axis intercept, respectively.[7,8] The ratio of stored charge contributed by capacitive process shown in the main text (Fig. 4d) is dominating at all the scan rates, which confirms the non-diffusion-controlled charge storage process of HATAQ. As the rate increases, a higher proportion of capacitive contribution is observed enabling an excellent rate performance.

Energy density calculation

The energy density of the HATAQ can be simplified as:[9,10]

$$E_{electrode} = C \times V_{average}$$

Where $E_{electrode}$ is energy density (Wh kg^{-1}); C is the maximum delivered capacity (mAh g^{-1}); $V_{average}$ is the average operating voltage.

Table S2. Organic-small-molecule cathode materials for non-aqueous Na-ion batteries reported in the literature.

Compound	**Electrode Composition** (**active material**: conductive carbon: binder)	**Electrolyte**	**Theoretical Capacity (Electron Transfer)**	**Voltage Window (V)**	**Initial Capacity at Lowest Rate Reported**	**Reversible Capacity at Highest Rate Reported**	**Capacity Retention at Highest Rate**	**Ref.**
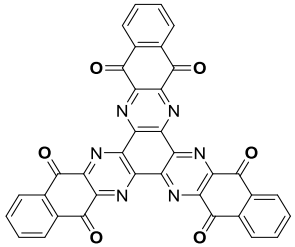	**HATAQ**:KB:PVDF (3:6:1)	0.9 M $NaPF_6$ in DEGDME	516 mAh g^{-1} (12 e^-)	0.9–3.7	460 mAh g^{-1} at 500 mA g^{-1}	138 mAh g^{-1} at 60 A g^{-1} (95 mAh g^{-1} at 80 A g^{-1} for 6 cycles)*	99 % after 5000 cycles and 93 % after 10000 cycles at 60 A g^{-1} (ED = 920 Wh kg^{-1})	This work
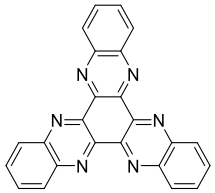	**TQA**:CB:PVDF (5:4:1)	1 M $NaPF_6$ in diglyme	418 mAh g^{-1} (6 e^-)	0.1–2.5	423 mAh g^{-1} at 100 mA g^{-1}	~224 mAh g^{-1} at 350 mA g^{-1}	85 % after 100 cycles at 350 mA g^{-1}	11
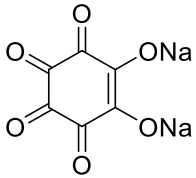	**$Na_2C_6O_6$**:AB:PVDF (7:2.5:0.5)	1 M $NaClO_4$ in PC	250 mAh g^{-1} (2 e^-)	1.0–3.2	270 mAh g^{-1} at 18 mA g^{-1}	n/a	n/a (ED = 370 Wh kg^{-1})	12

Compound	Electrode Composition (**active material**: conductive carbon: binder)	Electrolyte	Theoretical Capacity (Electron Transfer)	Voltage Window (V)	Initial Capacity at Lowest Rate Reported	Reversible Capacity at Highest Rate Reported	Capacity Retention at Highest Rate	Ref.
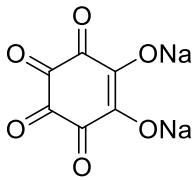	**SR**:CB:PVDF (7:2:1)	1 M $NaClO_4$ in 1:1 v/v EC/PC with 5% FEC	250 mAh g^{-1} (2 e^-)	1.6–2.8	190 mAh g^{-1} at 25 mA g^{-1}	n/a (95 mAh g^{-1} at 2.5 A g^{-1} for 5 cycles)*	n/a	13
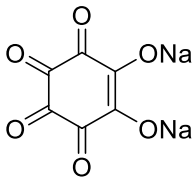	**$Na_2C_6O_6$**:Super P:PTFE (6:3:1)	0.6 M $NaPF_6$ in DEGDME	501 mAh g^{-1} (4 e^-)	0.5–3.3	498 mAh g^{-1} at 50 mA g^{-1}	n/a (371 mAh g^{-1} at 1 A g^{-1} for 3 cycles)*	n/a (ED = 726 Wh kg^{-1})	14
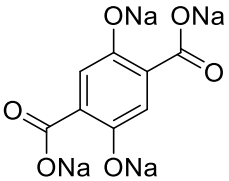	**$Na_2C_6O_6$**:Super P:PVDF (6.5:3:0.5)	1 M $NaClO_4$ in 1:1 v/v EC/DMC	187 mAh g^{-1} (2 e^-)	1.6–2.8	183 mAh g^{-1} at 19 mA g^{-1}	n/a (~80 mAh g^{-1} at 935 mA g^{-1} for 5 cycles)*	n/a	15

Compound	Electrode Composition (**active material**: conductive carbon: binder)	Electrolyte	Theoretical Capacity (Electron Transfer)	Voltage Window (V)	Initial Capacity at Lowest Rate Reported	Reversible Capacity at Highest Rate Reported	Capacity Retention at Highest Rate	Ref.
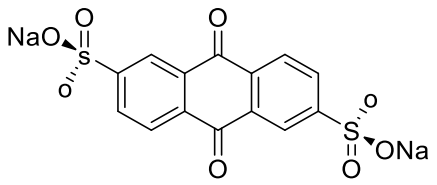	**Na_2AQ26DS**:KB+ CNTs:LA133+PVDF (7:2:1)	1 M $NaPF_6$ in DME	130 mAh g^{-1} (2 e^-)	0.5–3.2 (full cells)	131 mAh g^{-1} at 50 mA g^{-1}	n/a	n/a (ED = 157 Wh kg^{-1})	16
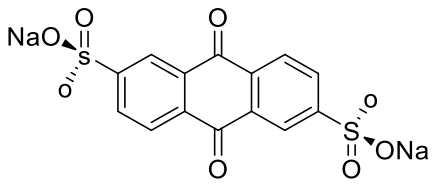	**Na_2AQ26DS**:KB:CNTs: LA133 (6:2:1:1)	1 M $NaPF_6$ in DME	130 mAh g^{-1} (2 e^-)	1.0–3.5	125 mAh g^{-1} at 50 mA g^{-1}	101 mAh g^{-1} at 1 A g^{-1} (86 mAh g^{-1} at 2 A g^{-1} for 5 cycles)*	72 % after 1000 cycles at 1 A g^{-1}	17
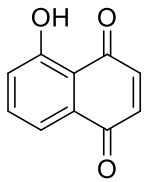	(**Juglone+RGO**):CB: PVDF (8:1:1)	1 M $NaClO_4$ in 1:1 v/v EC/DMC	290 mAh g^{-1} (2 e^-)	0.0–2.5	398 mAh g^{-1} at 50 mA g^{-1}	~400 mAh g^{-1} at 100 mA g^{-1} (210 mAh g^{-1} at 400 mA g^{-1} for 8 cycles)*	~76 % after 100 cycles at 100 mA g^{-1}	18

Compound	Electrode Composition (**active material**: conductive carbon: binder)	Electrolyte	Theoretical Capacity (Electron Transfer)	Voltage Window (V)	Initial Capacity at Lowest Rate Reported	Reversible Capacity at Highest Rate Reported	Capacity Retention at Highest Rate	Ref.
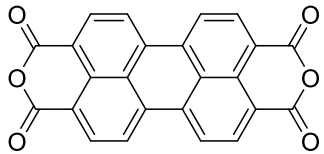	**PTCDA**:Super P:PVDF (7:2:1)	1 M $NaPF_6$ in 1:1 v/v EC/DEC	136 mAh g^{-1} (2 e^-)	1.0–3.0	134 mAh g^{-1} at 10 mA g^{-1}	~130 mAh g^{-1} at 200 mA g^{-1} (~90 mAh g^{-1} at 1 A g^{-1} for 1 cycle)*	~83 % after 200 cycles at 200 mA g^{-1}	19
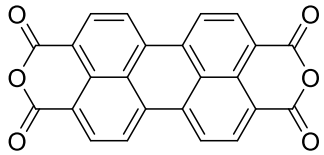	(**PTCDA+graphene aerogel**):AB:PVDF (8:1:1)	1 M $NaPF_6$ in 1:1 v/v EC/DMC	136 mAh g^{-1} (2 e^-)	1.5–3.5	98 mAh g^{-1} at 25 mA g^{-1}	~77 mAh g^{-1} at 100 mA g^{-1} (32 mAh g^{-1} at 2 A g^{-1} for 10 cycles)*	66.4 % after 1000 cycles at 100 mA g^{-1}	20
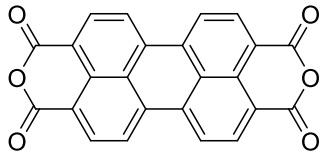	**PTCDA**:Super P:PVDF (8:1:1)	1 M $NaPF_6$ in 1:1 v/v EC/DMC	136 mAh g^{-1} (2 e^-)	1.5–3.5	56 mAh g^{-1} at 25 mA g^{-1}	n/a (48 mAh g^{-1} at 1 A g^{-1} for 10 cycles)*	n/a	21

Compound	Electrode Composition (**active material**: conductive carbon: binder)	Electrolyte	Theoretical Capacity (Electron Transfer)	Voltage Window (V)	Initial Capacity at Lowest Rate Reported	Reversible Capacity at Highest Rate Reported	Capacity Retention at Highest Rate	Ref.
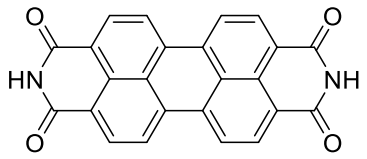	**PTCDI**:Super P:PTFE (8:1:1)	1 M $NaPF_6$ in 4.5:4.5:1 v/v/v EC/DEC/PC	135 mAh g^{-1} (2 e^-)	1.5–3.0	140 mAh g^{-1} at 10 mA g^{-1}	103 mAh g^{-1} at 600 mA g^{-1}	90 % after 300 cycles at 600 mA g^{-1}	22
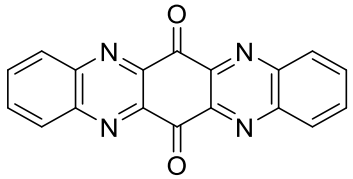	**TAPQ**:AB:CMC (7:2:1)	1 M $NaPF_6$ in DEGDME	515 mAh g^{-1} (6 e^-)	0.01–3.1	400 mAh g^{-1} at 50 mA g^{-1}	~350 mAh g^{-1} at 1 A g^{-1} (~240 mAh g^{-1} at 5 A g^{-1} for 10 cycles)*	72 % after 1000 cycles at 1 A g^{-1}	3
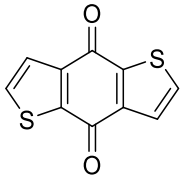	**BDT**:AB:PVDF (5:4:1)	1 M $NaClO_4$ in 1:1 v/v EC/DMC	243 mAh g^{-1} (2 e^-)	1.5–4.0	145 mAh g^{-1} at 24.3 mA g^{-1}	225 mAh g^{-1} at 48.6 mA g^{-1} (~79 mAh g^{-1} at 486 mA g^{-1} for 10 cycles)*	80 % after 70 cycles at 48.6 mA g^{-1}	23
	BDT-G:AB:PVDF (5:4:1)				217 mAh g^{-1} at 24.3 mA g^{-1}	220 mAh g^{-1} at 48.6 mA g^{-1} (~136 mAh g^{-1} at 486 mA g^{-1} for 10 cycles)*	45 % after 70 cycles at 48.6 mA g^{-1}	

Compound	Electrode Composition (**active material**: conductive carbon: binder)	Electrolyte	Theoretical Capacity (Electron Transfer)	Voltage Window (V)	Initial Capacity at Lowest Rate Reported	Reversible Capacity at Highest Rate Reported	Capacity Retention at Highest Rate	Ref.
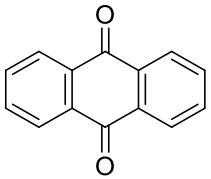	(**AQ/CMK-3**):Super P:PVDF ((4.5/4.5):0.5:0.5)	4 M $NaCF_3SO_3$ in triglyme	258 mAh g^{-1} (2 e^-)	1.2–2.8	214 mAh g^{-1} at 51.6 mA g^{-1}	n/a (143 mAh g^{-1} at 516 mA g^{-1} for 5 cycles)*	n/a	24
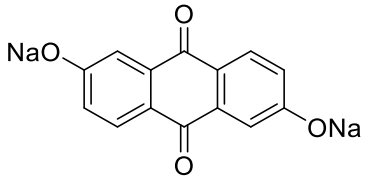	**AQ26ONa**:KB:CNTs: PVDF (6:2:1:1)	1 M $NaPF_6$ in DME	189 mAh g^{-1} (2 e^-)	0.2–3.3	245 mAh g^{-1} at 50 mA g^{-1}	154 mAh g^{-1} at 500 mA g^{-1}	66 % after 2500 cycles at 500 mA g^{-1} (ED = 102 Wh kg^{-1})	25
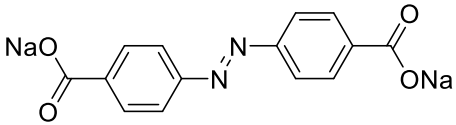	**ADASS**:CB:SA (6:3:1)	1 M $NaPF_6$ in DEGDME	170 mAh g^{-1} (2 e^-)	0.5–2.0	170 mAh g^{-1} at 34 mA g^{-1}	~105 mAh g^{-1} at 3.4 A g^{-1} (~71 mAh g^{-1} at 6.8 A g^{-1} for 5 cycles)*	~99 % after 2000 cycles at 3.4 A g^{-1}	26

Compound	Electrode Composition (**active material**: conductive carbon: binder)	Electrolyte	Theoretical Capacity (Electron Transfer)	Voltage Window (V)	Initial Capacity at Lowest Rate Reported	Reversible Capacity at Highest Rate Reported	Capacity Retention at Highest Rate	Ref.
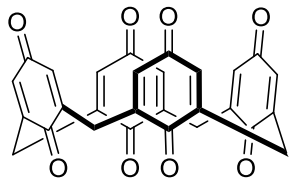	(**C4Q/CMK-3**): Super P:PVDF ((4/4):0.5:1.5)	1 M $NaClO_4$ in 1:1 v/v EC/DMC with 5% FEC	446 mAh g^{-1} (8 e^-)	1.2–4.2	438 mAh g^{-1} at 44.6 mA g^{-1}	n/a (130.4 mAh g^{-1} at 446 mA g^{-1} for 4 cycles)*	n/a	27
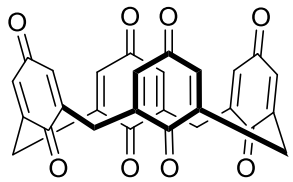	(**C4Q/CMK-3**): SWCNTs:PVDF ((4/4):1:1)	1 M $NaClO_4$ in 1:1 v/v EC/DMC with 5% FEC	446 mAh g^{-1} (8 e^-)	1.2–4.2	441 mAh g^{-1} at 44.6 mA g^{-1}	n/a (346 mAh g^{-1} at 446 mA g^{-1} for 4 cycles)*	n/a	28
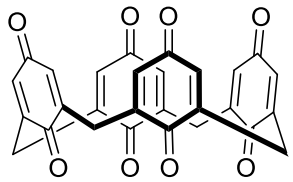	**C4Q**:PPL:PVDF (4.5:4.5:1)	1 M $NaClO_4$ in 1:1 v/v EC/DEC with 5% FEC	446 mAh g^{-1} (8 e^-)	1.2–4.2	435 mAh g^{-1} at 44.6 mA g^{-1}	n/a (346 mAh g^{-1} at 446 mA g^{-1} for 4 cycles)*	n/a	29

Compound	Electrode Composition (**active material**: conductive carbon: binder)	Electrolyte	Theoretical Capacity (Electron Transfer)	Voltage Window (V)	Initial Capacity at Lowest Rate Reported	Reversible Capacity at Highest Rate Reported	Capacity Retention at Highest Rate	Ref.
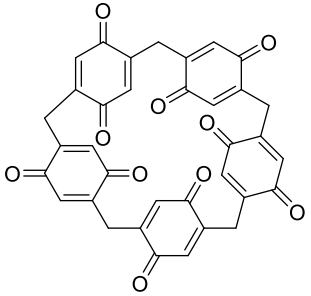	(**P5Q/CMK-3**): SWCNTs:PVDF ((2/4):3:1)	1 M $NaClO_4$ in 1:1 v/v EC/DMC with 5% FEC	446 mAh g^{-1} (10 e^-)	1.5–4.2	418 mAh g^{-1} at 44.6 mA g^{-1}	n/a (201 mAh g^{-1} at 446 mA g^{-1} for 4 cycles)*	n/a	30
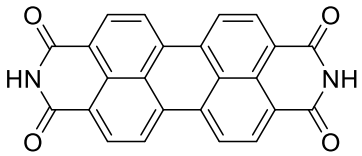	**PDI**:AB:PVDF (6:3:1)	1 M $NaPF_6$ in PC	91 mAh g^{-1} (2 e^-)	1.5–3.0	77 mAh g^{-1} at 20 mA g^{-1}	n/a	n/a	31
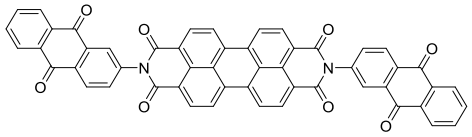	**PTCDI-DAQ**:KB:LA133 (6:3:1)	4 M $NaPF_6$ in DME	200 mAh g^{-1} (6 e^-)	1.0–3.5	206 mAh g^{-1} at 100 mA g^{-1}	n/a (125 mAh g^{-1} at 10 A g^{-1} for 1 cycle)*	n/a (ED = 247 Wh kg^{-1})	32

Compound	Electrode Composition (**active material**: conductive carbon: binder)	Electrolyte	Theoretical Capacity (Electron Transfer)	Voltage Window (V)	Initial Capacity at Lowest Rate Reported	Reversible Capacity at Highest Rate Reported	Capacity Retention at Highest Rate	Ref.
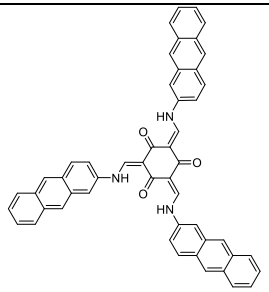	**TSAA**:Super P:PVDF (6:3:1)	1 M $NaClO_4$ in 1:1 v/v EC/DMC	109 mAh g^{-1} (3 e^-)	0.05–3.0	187 mAh g^{-1} at 50 mA g^{-1}	n/a (95 mAh g^{-1} at 1 A g^{-1} for 7 cycles)*	n/a	33
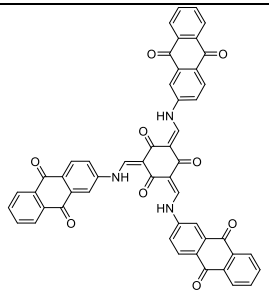	**TSAQ**:Super P:PVDF (6:3:1)		292 mAh g^{-1} (9 e^-)		320 mAh g^{-1} at 50 mA g^{-1}	218 mAh g^{-1} at 1 A g^{-1}	~110 % after 2500 cycles at 1 A g^{-1}	
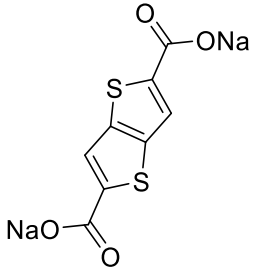	**STTDC**:Super P:SA (6:3:1)	1 M $NaClO_4$ in 1:1 v/v EC/PC with 5% FEC	591 mAh g^{-1} (6 e^-)	0.01–3.0	426 mAh g^{-1} at 50 mA g^{-1}	~100 mAh g^{-1} at 5 A g^{-1}	~194 % after 4000 cycles at 5 A g^{-1}	34

Compound	Electrode Composition (**active material**: conductive carbon: binder)	Electrolyte	Theoretical Capacity (Electron Transfer)	Voltage Window (V)	Initial Capacity at Lowest Rate Reported	Reversible Capacity at Highest Rate Reported	Capacity Retention at Highest Rate	Ref.
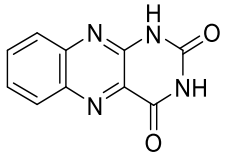	**ALX**:Super P:PTFE (4:4:2)	1 M $NaPF_6$ in DEGDME	250 mAh g^{-1} (2 e^-)	1.2–3.3	168 mAh g^{-1} at 10 mA g^{-1}	n/a	n/a	35
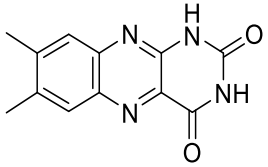	**LC**:Super P:PTFE (4:4:2)		221 mAh g^{-1} (2 e^-)	1.2–3.3	138 mAh g^{-1} at 10 mA g^{-1}	n/a	n/a	
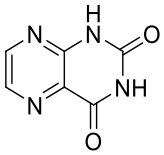	**LMZ**:Super P:PTFE (4:4:2)		327 mAh g^{-1} (2 e^-)	1.2–3.6	70 mAh g^{-1} at 10 mA g^{-1}	n/a	n/a	

Compound	Electrode Composition (**active material**: conductive carbon: binder)	Electrolyte	Theoretical Capacity (Electron Transfer)	Voltage Window (V)	Initial Capacity at Lowest Rate Reported	Reversible Capacity at Highest Rate Reported	Capacity Retention at Highest Rate	Ref.
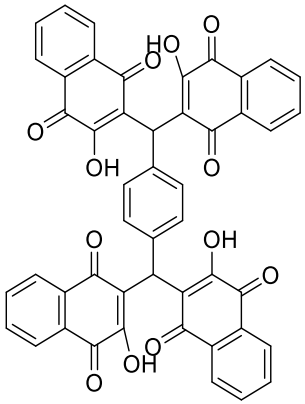	**TKL**:Super C65 (6:4)	1 M $NaClO_4$ in DEGDME	101 mAh g^{-1} (3 e^-)	1.3–3.0	237 mAh g^{-1} at 50 mA g^{-1}	n/a (~40 mAh g^{-1} at 1 A g^{-1} for 5 cycles)*	n/a	36

Note: * indicates capacity taken from the rate capability plot or the discharge/charge profile. ED = energy density; KB = Ketjen black; CB = carbon black; AB = acetylene black; CNTs = carbon nanotubes; CMK-3 = ordered mesoporous carbon; SWCNTs = single wall carbon nanotubes; PPL = Physalis Peruviana L. Calyx; PVDF = polyvinylidene fluoride; PTFE = polytetrafluoroethylene; LA133 = polyacrylonitrile copolymer; CMC = carboxymethyl cellulose; SA = sodium alginate; EC = ethylene carbonate; DMC = dimethyl carbonate; DME = dimethoxyethane, also known as monoglyme or ethylene glycol dimethyl ether; PC = propylene carbonate; DEC = diethyl carbonate; DEGDME = diethylene glycol dimethyl ether or diglyme; triglyme = triethylene glycol dimethyl ether; FEC = fluoroethylene carbonate.

References

(1) Jiang, Q; Xiong, P.; Liu, J.; Xie, Z.; Wang, Q.; Yang, X.-Q.; Hu, E.; Cao, Y.; Sun, J.; Xu, Y.; Chen, L. A Redox-Active 2D Metal–Organic Framework for Efficient Lithium Storage with Extraordinary High Capacity. *Angew. Chem., Int. Ed.* **2020**, 59, 5273–5277.

(2) Cook, J. B.; Kim, H.-S.; Lin, T. C.; Lai, C.-H.; Dunn, B.; Tolbert, S. H. Pseudocapacitive Charge Storage in Thick Composite MoS_2 Nanocrystal-Based Electrodes. *Adv. Energy Mater.* **2017**, *7*, 1601283.

(3) Sun, T.; Feng, X.-L.; Sun, Q.-Q.; Yu, Y.; Yuan, G.-B.; Xiong, Q.; Liu, D.-P.; Zhang, X.-B.; Zhang, Y. Solvation Effect on the Improved Sodium Storage Performance of N-Heteropentacenequinone for Sodium-Ion Batteries. *Angew. Chem., Int. Ed.* **2021**, *60*, 26806–26812.

(4) Yang, J.; Ruan, J.; Li, Q.; Fang, F.; Song, Y.; Sun, D.; Wang, F. Improved Low-Temperature Performance of Rocking-Chair Sodium-Ion Hybrid Capacitor by Mitigating the De-Solvation Energy and Interphase Resistance. *Adv. Funct. Mater.* **2022**, DOI: 10.1002/adfm.202200566.

(5) Xu, K.; Lam, Y.; Zhang, S. S.; Jow, T. R.; Curtis, T. B. Solvation Sheath of Li^+ in Nonaqueous Electrolytes and Its Implication of Graphite/Electrolyte Interface Chemistry. *J. Phys. Chem. C* **2007**, *111*, 7411–7421.

(6) Xu, K. "Charge-Transfer" Process at Graphite/Electrolyte Interface and the Solvation Sheath Structure of Li^+ in Nonaqueous Electrolytes. *J. Electrochem. Soc.* **2007**, 154, A162–A167.

(7) Wang, J.; Polleux, J.; Lim, J.; Dunn, B. Pseudocapacitive Contributions to Electrochemical Energy Storage in TiO_2 (Anatase) Nanoparticles. *J. Phys. Chem. C* **2007**, *111*, 14925–14931.

(8) Lim, E.; Jo, C.; Kim, H.; Kim, M.-H.; Mun, Y.; Chun, J.; Ye, Y.; Hwang, J.; Ha, K.-S.; Roh, K. C.; Kang, K.; Yoon, S.; Lee, J. Facile Synthesis of Nb_2O_5@Carbon Core–Shell Nanocrystals with Controlled Crystalline Structure for High-Power Anodes in Hybrid Supercapacitors. *ACS Nano*, **2015**, *9*, 7497–7505.

(9) Peng, C.; Ning, G.-H.; Su, J.; Zhong, G.; Tang, W.; Tian, B.; Su, C.; Yu, D.; Zu, L.; Yang, J.; Ng, M.-F.; Hu, Y.-S.; Yang, Y.; Armand, M.; Loh, K. P. Reversible Multi-electron Redox Chemistry of π-conjugated N-containing Heteroaromatic Molecule-based Organic Cathodes. *Nat. Energy*, **2017**, *2*, 17074.

(10) Ji, H.; Wu, J.; Cai, Z.; Liu, J.; Kwon, D.-H.; Kim, H.; Urban, A.; Papp, J. K.; Foley, E.; Tian, Y.; Balasubramanian, M.; Kim, H.; Clément, R. J.; McCloskey, B. D.; Yang, W.; Ceder, G. Ultrahigh Power and Energy Density in Partially Ordered Lithium-Ion Cathode Materials. *Nat. Energy*, **2020**, *5*, 213–221.

(11) Zhao, Q.; Zhao, W.; Zhang, C.; Wu, Y.; Yuan, Q.; Whittaker, A. K.; Zhao, X.

Sodium-Ion Storage Mechanism in Triquinoxalinylene and a Strategy for Improving Electrode Stability. *Energy Fuels* **2020,** *34*, 5099–5105.
(12) Chihara, K.; Chujo, N.; Kitajou, A.; Okada, S. Cathode Properties of $Na_2C_6O_6$ for Sodium-Ion Batteries. *Electrochim. Acta* **2013,** *110*, 240–246.
(13) Wang, Y.; Ding, Y.; Pan, L.; Shi, Y.; Yue, Z.; Shi, Y.; Yu, G. Understanding the Size-dependent Sodium Storage Properties of $Na_2C_6O_6$-based Organic Electrodes for Sodium-Ion Batteries. *Nano Lett.* **2016,** *16*, 3329–3334.
(14) Lee, M.; Hong, J.; Lopez, J.; Sun, Y.; Feng, D.; Lim, K.; Chueh, W. C.; Toney, M. F.; Cui, Y.; Bao, Z. High-performance Sodium–Organic Battery by Realizing Four-sodium Storage in Disodium Rhodizonate. *Nat. Energy* **2017,** *2*, 861–868.
(15) Wang, S.; Wang, L.; Zhu, Z.; Hu, Z.; Zhao, Q.; Chen, J. All Organic Sodium-Ion Batteries with $Na_4C_8H_2O_6$. *Angew. Chem., Int. Ed.* **2014,** *126*, 6002–6006.
(16) Li, D.; Tang, W.; Yong, C. Y.; Tan, Z. H.; Wang, C.; Fan, C. Long-lifespan Polyanionic Organic Cathodes for Highly Efficient Organic Sodium-Ion Batteries. *ChemSusChem* **2020,** *13*, 1991–1996.
(17) Tang, W.; Liang, R.; Li, D.; Yu, Q.; Hu, J.; Cao, B.; Fan, C. Highly Stable and High Rate-Performance Na-Ion Batteries Using Polyanionic Anthraquinone as the Organic Cathode. *ChemSusChem* **2019,** *12*, 2181–2185.
(18) Wang, H.; Hu, P.; Yang, J.; Gong, G.; Guo, L.; Chen, X. Renewable-juglone-based High-performance Sodium-Ion Batteries. *Adv. Mater.* **2015,** *27*, 2348–2354.
(19) Luo, W.; Allen, M.; Raju, V.; Ji, X. An Organic Pigment as a High-performance Cathode for Sodium-Ion Batteries. *Adv. Energy Mater.* **2014,** *4*, 1400554.
(20) Yuan, C.; Wu, Q.; Li, Q.; Duan, Q.; Li, Y.; Wang, H.-g. Nanoengineered Ultralight Organic Cathode Based on Aromatic Carbonyl Compound/graphene Aerogel for Green Lithium and Sodium Ion Batteries. *ACS Sustain. Chem. Eng.* **2018,** *6*, 8392–8399.
(21) Yuan, C.; Wu, Q.; Shao, Q.; Li, Q.; Gao, B.; Duan, Q.; Wang, H.-G. Free-standing and Flexible Organic Cathode Based on Aromatic Carbonyl Compound/Carbon Nanotube Composite for Lithium and Sodium Organic Batteries. *J. Colloid Interface Sci.* **2018,** *517*, 72–79.
(22) Deng, W.; Shen, Y.; Qian, J.; Cao, Y.; Yang, H. A Perylene Diimide Crystal with High Capacity and Stable Cyclability for Na-Ion Batteries. *ACS Appl. Mater. Interfaces* **2015,** *7*, 21095–21099.
(23) Chen, X.; Wu, Y.; Huang, Z.; Yang, X.; Li, W.; Yu, L. C.; Zeng, R.; Luo, Y.; Chou, S.-L. $C_{10}H_4O_2S_2$/graphene Composite as a Cathode Material for Sodium-Ion Batteries. *J. Mater. Chem. A* **2016,** *4*, 18409–18415.
(24) Guo, C.; Zhang, K.; Zhao, Q.; Pei, L.; Chen, J. High-performance Sodium Batteries with the 9,10-anthraquinone/CMK-3 Cathode and an Ether-based Electrolyte. *Chem. Commun.* **2015,** *51*, 10244–10247.

(25) Hu, J.; Liang, R.; Tang, W.; He, H.; Fan, C. Synthesis of Polyanionic Anthraquinones as New Insoluble Organic Cathodes for Organic Na-Ion Batteries. *Int. J. Hydrog. Energy* **2020,** *45*, 24573–24581.
(26) Luo, C.; Xu, G. L.; Ji, X.; Hou, S.; Chen, L.; Wang, F.; Jiang, J.; Chen, Z.; Ren, Y.; Amine, K. Reversible Redox Chemistry of Azo Compounds for Sodium-Ion Batteries. *Angew. Chem., Int. Ed.* **2018,** *57*, 2879–2883.
(27) Zheng, S.; Hu, J.; Huang, W. An Inorganic–Organic Nanocomposite Calix[4] quinone (C4Q)/CMK-3 as a Cathode Material for High-capacity Sodium Batteries. *Inorg. Chem. Front.* **2017,** *4*, 1806–1812.
(28) Yan, B.; Wang, L.; Huang, W.; Zheng, S.; Hu, P.; Du, Y. High-capacity Organic Sodium Ion Batteries using a Sustainable C4Q/CMK-3/SWCNT Electrode. *Inorg. Chem. Front.* **2019,** *6*, 1977–1985.
(29) Zhou, W.; Zhang, X.; Zhang, W.; Huang, W.; Yan, B.; Li, H.; Yu, S. Combination of High Performance Organic Cathode Calix[4]quinone and Practical Biocarbon in Sodium-Ion Batteries. *Org. Electron.* **2020,** *82*, 105702.
(30) Xiong, W.; Huang, W.; Zhang, M.; Hu, P.; Cui, H.; Zhang, Q. Pillar[5]quinone–Carbon Nanocomposites as High-capacity Cathodes for Sodium-Ion Batteries. *Chem. Mater.* **2019,** *31*, 8069–8075.
(31) Banda, H.; Damien, D.; Nagarajan, K.; Raj, A.; Hariharan, M.; Shaijumon, M. M. Twisted Perylene Diimides with Tunable Redox Properties for Organic Sodium-Ion Batteries. *Adv. Energy Mater.* **2017,** *7*, 1701316.
(32) Hu, Y.; Yu, Q.; Tang, W.; Cheng, M.; Wang, X.; Liu, S.; Gao, J.; Wang, M.; Xiong, M.; Hu, J. Ultra-stable, Ultra-long-lifespan and Ultra-high-rate Na-Ion Batteries Using Small-molecule Organic Cathodes. *Energy Storage Mater.* **2021,** *41*, 738–747.
(33) Wu, S.; Wang, W.; Li, M.; Cao, L.; Lyu, F.; Yang, M.; Wang, Z.; Shi, Y.; Nan, B.; Yu, S. Highly Durable Organic Electrode for Sodium-Ion Batteries via a Stabilized α-C Radical Intermediate. *Nat. Commun.* **2016,** *7*, 13318.
(34) Ma, C.; Wang, L.-Y.; Shu, M.-H.; Hou, C.-C.; Wang, K.-X.; Chen, J.-S. Thiophene Derivatives as Electrode Materials for High-performance Sodium-Ion Batteries. *J. Mater. Chem. A* **2021,** *9*, 11530–11536.
(35) Hong, J.; Lee, M.; Lee, B.; Seo, D.-H.; Park, C. B.; Kang, K. Biologically Inspired Pteridine Redox Centres for Rechargeable Batteries. *Nat. commun.* **2014,** *5*, 5335.
(36) Miroshnikov, M.; Kato, K.; Babu, G.; Kumar, N.; Mahankali, K.; Hohenstein, E.; Wang, H.; Satapathy, S.; Divya, K. P.; Asare, H. Nature-derived Sodium-Ion Battery: Mechanistic Insights into Na-Ion Coordination Within Sustainable Molecular Cathode Materials. *ACS Appl. Energy Mater.* **2019,** *2*, 8596–8604.